PNAS
www.pnas.org

Supplementary Information for

3d virtual histology of the human hippocampus based on phase-contrast computed-tomography

M. Eckermann, B. Schmitzer, F. van der Meer†, J. Franz, O. Hansen, C. Stadelmann, T. Salditt

Tim Salditt.
E-mail: tsaldit@gwdg.de

This PDF file includes:

Supplementary text
Figs. S1 to S7 (not allowed for Brief Reports)
Tables S1 to S3 (not allowed for Brief Reports)
SI References

Supporting Information Text

SI Methods

Sample Collection and Preparation Human hippocampus tissue was retrieved at routine autopsy in agreement with the ethics committee of the University Medical Center Göttingen. Following the protocol from clinical pathology routine, autopsy dissection blocks from 23 subjects (13 subjects for DG-samples only, 2 for CA1-samples only, 6 for DG- and CA1-samples, 1 for DG-, CA1- and WM-samples, and 1 subject for GM-sample; in total resulting in 20 DG-samples, 4 CA1-samples, 1 WM- and 1 GM-sample) were 10% PFA-fixed, dehydrated and paraffin-embedded (FFPE). One FFPE block measures about $2 \times 3 \times 0.3$ cm^3. Tab. S1 lists the sample numbers with neuropathological staging. Tissue of one further patient has been 10% PFA-fixed and stored in PBS, i.e. has not been dehydrated and paraffin-embedded, for hydrated examination (cf. Fig. S6). For PC-CT, cylindrical samples were extracted using either a 1 or 8 mm-biopsy punch and inserted into polyimide tubes. A note on the number of DG samples: during the analysis of CB data from DG samples, 3/20 needed to be excluded since the corresponding tomographic acquisitions yielded inferior data quality and the automated segmentation quality was hence not on a comparable level (this concerns subjects 4, 9 and 20), while this was not necessary for PB data, which is much more robust against beam fluctuations.

Neuropathological Staging Patients were diagnosed as AD patients following post-mortem analysis according to (1–4). Intraneuronal tangles as well as dystrophic neuritic plaques were analyzed in hippocampal, temporal, frontal and occipital sections stained with a phospho-tau antibody (monoclonal mouse at8, Thermo Fisher Scientific, 1:100, pretreatment steamer + citrate pH 6). The same hippocampal blocks were used for neuropathological staging and PC-CT. For staging of plaques, Bielschowsky silver impregnation and an amyloid-beta staining (monoclonal mouse anti amyloid-beta, 6E10, Zytomed Systems GmbH, 1:500 after pretreatment with formic acid, steamer + citrate pH 6) were performed. Following (4), we then classified patients according to the ABC score, accounting for β-amyloid plaques according to Thal phases (1) (A), neurofibrillar tangles according to Braak stages (2, 5) (B), and for neuritic plaques according to the CERAD score (3) (C). The overall ABC score is then evaluated in terms of an AD likelihood based on a logic matrix with the individual entries, as defined in (4). In this work, patients with a AD likelihood "intermediate" or "high" according to the compound ABC score were classified as AD patients, again following (4). One subject showed an amyloid pathology with cerebral amyloid angiopathy only while another subject displayed tau pathology only, with almost no amyloid depositions (subjects 12 and 13, respectively). Both are not assigned to any group. All results of the neuropathological staging are tabulated Tab. S1.

Experimental Setup The data presented in this work were recorded at the GINIX holo-tomography endstation of the P10 undulator beamline, Petra III, DESY, Hamburg (6), at a photon energy of 8.0 and 13.8 keV, selected by a Si(111) channel-cut monochromator. The beamline's high brilliance $> 10^{21}$ ph/s $mrad^2$ mm^2 (0.1% BW) (7), and correspondingly high coherence, enables coherent nano-focusing, and hence high-resolution phase-contrast recordings in the holographic regime, as well as high-contrast and fast parallel-beam acquisitions. In order to cover the cytoarchitecture over a wide range of length scales, ranging from the entire hippocampus structure in frontal plane, down to regions-of-interest (ROIs) within the dentate gyrus at sub-cellular resolution, the instrument's multiscale capability was used (8, 9), comprising three different optical configurations which are illustrated in Fig. S1. First, large field-of-views (FOVs) of up to about 8 mm were scanned in a beam which was focused by a Kirkpatrick-Baez (KB) mirror system and subsequently broadened by its divergence. This is denoted as expanded beam (EB) configuration. Second, intermediate FOVs of up to about 1.5 mm were scanned in a parallel beam (PB) configuration, after moving the mirrors out of the beam path. Finally, small FOVs of up to about 0.4 mm were scanned at highest resolution, using a compound optics of KB mirrors and X-ray waveguides (WG) (10, 11) (cone-beam configuration, CB). By adjusting the distance z_{01} between WG and sample, two different voxel sizes of $px \simeq 160$ nm and $px \simeq 50$ nm were chosen in this configuration, providing further zoom. The reconstructed volumes of all recordings could be precisely registered with respect to each other, enabling a zoom into specific ROIs. The three configurations with their respective optical components, detector technologies, and tomographic acquisition schemes are presented in Tab. S2, and described in more detail below.

EB Configuration X-rays were focused by Kirkpatrick-Baez (KB) mirrors onto a 3 µm pinhole, fabricated by focused-ion-milling, and acting as a spatial filter. This helped to suppress the stripe artifacts typically associated with the KB farfield (9). The sample stage was installed in the expanded beam at $z_{01} \approx 5.1$ m behind the focus. The projections were recorded with a sCMOS detector (pco.edge, Optique Peter, 50 µm-LuAg scintillator, 6.5 µm physical pixel size and 2× interchangeable lenses) at a position of $z_{02} \approx 5.4$ m. This configuration was used for PC-CT measurements of a 8 mm cylindrical tissue sample, covering the characteristic anatomical regions, notably the DG and the CA. The sample fit entirely into the FOV 8.3 mm×6.7 mm. Data from this configuration are presented in Fig. 1(c), where the CA1-4 fields, the DG, WM and further GM as well as vasculature can be clearly identified.

PB Configuration After removing the KB mirrors, the pinhole, as well as various foils and windows of the beamline (8), the parallel undulator beam was used for PC-CT (Fig. S1). The sample was installed on a fully motorized tomography stage with air bearing (UPR-160 Air, Micos, Germany). Given the accuracy and reproducibility of the rotation, it was possible to acquire projections in a continuous scan, i.e. projections with a short exposure time were taken during continuous rotation of the sample (8). 1501 projections were acquired at a propagation distance $z_{12} = 220$ mm with an acquisition time of 0.035 s, using the microscope camera system described above with the 10× objective. This resulted in a FOV of 1.7 mm×1.3 mm at 0.65 µm voxel size. This configuration was used both for punch biopsies of 1 mm diameter covered in a single scan, as well as to map multi-mm sized tissue samples by stitching and merging of several individual tomograms (Fig. 2).

Table S1. Sample list for neuropathological analysis: Columns give the assignment of sample numbers in the manuscript, the age, the A (Aβ plaque score), B (NFT stage) and C (Neuritic plaque score), with the Thal phases (1), the Braak stage (2) and the CERAD score (3), respectively, the cerebral amyloid angiopathy (CAA) and the overall ABC score according to (4), as well as the group assignment based on ABC and, finally, which hippocampal region has been analyzed from the respective subject.

Subject no.	Age	Thal phase	A	Braak stage	B	CERAD score	C	CAA	ABC-based scoring	Group	Sex	PC-CT analysis of...
1	82	3	A2	3	B2	sparse	C1	1	intermediate†	AD	f	DG
2	71	4-5	A3	5	B3	frequent	C3	0	high†	AD	m	DG & CA1
3	74	3	A2	6	B3	moderate	C2	1	intermediate	AD	f	DG
4	84	3	A2	4	B2	sparse	C1	0	intermediate†	AD	m	DG*
5	66	4-5	A3	6	B3	frequent	C3	1	high†	AD	m	DG
6	72	3	A2	6	B3	moderate	C2	0	intermediate	AD	m	DG & CA1
7	83	1-2	A1	5	B3	moderate	C2	1	intermediate†	AD	f	DG
8	91	4-5	A3	6	B3	frequent	C3	1	high†	AD	m	DG
9	70	3	A2	5	B3	moderate	C2	1	intermediate	AD	f	DG*
10	62	4-5	A3	4	B2	moderate	C2	0	intermediate	AD	f	DG
11	87	3	A2	5	B3	sparse	C1	1	intermediate	AD	f	DG
12	86	0	A0	5	B3	not	C0	1	not	-	m	DG & CA1
13	87	1-2	A1	4	B2	not	C0	0	low	-	f	DG
14	84	0	A0	2	B1	not	C0	0	not	CTRL	f	DG
15	77	3	A2	2	B1	not	C0	0	low	CTRL	m	DG
16	74	1-2	A1	2	B1	not	C0	0	low	CTRL	f	DG & CA1
17	71	1	A1	1	B1	nd	nd	nd	N-L	CTRL	m	DG & CA1
18	65	0	A0	1	B1	not	C0	0	not	CTRL	m	DG
19	83	3	A2	1	B1	sparse	C1	0	low	CTRL	m	DG
20	82	0	A0	2	B1	not	C0	0	not	CTRL	m	DG* & CA1
21	91	4-5	A3	5	B3	moderate	C2	0	intermediate	AD	m	CA1
22	37	0	A0	1	B1	sparse	C0	0	not	CTRL	m	CA1

† marks a known clinical history of dementia, * the CB data sets which have been excluded from analysis. nd = not determined.

CB Configuration For cone-beam (CB) PC-CT with high spatial resolution, the beam was focused by KB mirrors to approx. 310×320 nm^2, and coupled into an X-ray waveguide (WG) for further reduction of beam size, and for coherence and wavefront filtering. The waveguides consist of empty channels (10^2 nm lateral entrance/exit width) fabricated by e-beam lithography and wafer bonding (12–15). At low-E X-rays (i.e. $\leq$ 8 keV), a WG with a 1 mm-guiding layer consisting of Si was selected, at high-E X-rays ($\geq$ 13.8 keV), Ge was chosen with 0.2 mm depth; see also Tab. S2 for specifications of the WG systems. The WG provides a secondary source of sub-50 nm spot size, and a beam with high spatial coherence and a smooth wavefront, which is decoupled from upstream optical components of the beamline. The geometric magnification of $M = \frac{z_{02}}{z_{01}} \approx 41$, or $M \approx 132$, respectively, was adjusted by the motorized sample tower (same as PB configuration). Projections were recorded with a fiber-coupled sCMOS Camera (Zyla 5.5 HF, Andor) positioned at $z_{02} \approx 5.1$ m, with 2560 $\times$ 2160 pixels of 6.5 µm pixel size, and 15 µm-Gadox scintillator. Biopsy punches of 1 mm cross section were scanned with a FOV of 0.4 mm$\times$0.4 mm and a voxel sizes of approx. 160 nm (values for $M \approx 41$), which allowed investigations with sub-cellular resolution, regarding in particular the structure of the DG cell nuclei (cf. Fig. 2(b & c)).

Phase Retrieval and Object Reconstruction Phase retrieval has been carried out after correcting for empty beam and dark images, recorded before and after the tomography scans. For the EB configuration, empty beam recordings were analyzed by *principal component analysis* (PCA) prior to flat-field correction (9). Phase retrieval was performed by either the linearized *contrast-transfer-function* (CTF) scheme or by the *non-linear Tikhonov* (NLT) algorithm (16). Both are well-suited for the holographic regime corresponding to image formation at small Fresnel numbers $F = \frac{px^2}{z_{\text{eff}}\lambda} \ll 1$, with wavelength λ, and the effective propagation distance $z_{\text{eff}} = z_{12}/M$. For homogeneous objects with coupled ratio $\frac{\delta}{\beta}$ of the decrements of the index of refraction $n = 1 - \delta + i\beta$, the phase Φ in the object plane is obtained from the flat-field corrected projections I_{exp} by (17–19)

$$\Phi(\vec{r_\perp}) = {\mathcal{F}_\perp}^{-1}\left(\frac{\sum_{n=1}^{N}\xi_n \cdot \mathcal{F}_\perp\left(I_{\text{exp}}(\vec{r}_\perp, z_n) - 1\right)}{\sum_{n=1}^{N} 2\cdot\xi_n^2 + \alpha(\vec{k}_\perp)}\right) , \qquad [1]$$

$$\xi_n = \sin(\chi_n) + \frac{\delta}{\beta}\cos(\chi_n) ,$$

where $\vec{r}_\perp$ denotes the position vector in the object plane, and $\vec{k}$ the squared spatial frequency in natural units $\chi_n = \frac{\lambda_n z_n k_{x,y}^2}{4\pi}$. In phase retrieval, the optical property of the tissue $\frac{\delta}{\beta}$ is treated as an effective parameter, chosen based on inspection. The zero-crossings of the denominator are regularized by the function $\alpha(\vec{k}_\perp)$. To further stabilize phase retrieval, multiple datasets (N = 2-4) at different, carefully chosen χ_n were recorded, based on variation of z_{01}. When the linearization inherent in CTF-reconstruction failed, we utilized the iterative NLT-algorithm which can be regarded as a non-linear generalization (16). In fact, the NLT was used for most of the data collected in CB configuration, in particular the entire scan series used for the statistical DG analysis. After phase retrieval of the projections, tomographic reconstruction was performed by filtered back-projection (FBP), or a cone-beam (FDK) algorithm, both as implemented in the ASTRA-toolbox (20–22). Post-processing included a ring-filter step as in (23) ("additive"/"A" approach) or (24) ("wavelet"/"W"). Alternatively, in the datasets of PB configuration which encompassed full 360°-scans, ring artifacts were treated by respective "replacement" ("R"). Spatial resolution was determined using Fourier-Shell-correlation (FSC) (25), after applying a Kaiser-Bessel-window of 7 pixels and a half-bit threshold. If desired, gray values could be converted to electron density ρ ($e^-/\mu m^3$) using tabulated values (26) as detailed in (27), based on the X-ray energy and the fact that the tissues were fully penetrated by paraffin ($C_{30}H_{62}$, 0.9 g/cm^3, $\rho \approx 3.1 \cdot 10^2$ nm^{-3}, under the assumption that the maximum of the tomographic gray value histogram can be assigned to the impregnation material). Based on the image quality metrics, 2/10 AD subjects and 1/10 control CB datasets were excluded from the analysis to keep the segmentation quality on a similar level for all data sets (subjects 4, 9 and 20).

Segmentation of CA1 Neurons Segmentation of pyramidal neurons in the CA1 region required a segmentation algorithm compatible with low contrast and variable cellular morphology. At the same time, there was not sufficient data available for the deep learning approach, as used for the DG cell nuclei. We therefore turned to the *Chan-Vese level-set* algorithm (28), which determines the object contour (mask) based on minimizing an energy functional, including contributions due to gray value deviations from the average values in- and outside the object, its surface and its volume. In this work, the python level-set implementation of the *simple insight toolkit* (29) was used.

Computation of Local Cell Density Using the segmentation masks, each single object (i.e. cell nucleus) was identified and represented by its center-of-mass (COM). The resulting 3d-array M_p hence has non-zero entries only at the COM positions. The local density on a given coarse-graining scale r was then computed by convolution between COM-positions and a sphere with radius r. The local density at any point is proportional to the number of spheres reaching this point and the volume of the test sphere. To avoid artifacts from sharp interfaces, the spheres were smoothed by Gaussian filtering. Denoting the smoothed sphere (convolution kernel) as M_r, the convolution is implemented in Fourier space based on multiplication of the *Fast Fourier transforms* (FFT) of M_p and M_r. The cell density ρ_{pr} (objects per volume element) in real space is then obtained by the inverse FFT followed by a proper normalization, which can be written as

$$\rho_{pr} = \frac{1}{px^3} \cdot \frac{\Re\left(\mathcal{F}^{-1}\left(\mathcal{F}(M_p)\cdot\mathcal{F}(M_r)\right)\right)}{\Re\left(\mathcal{F}^{-1}\left(\mathcal{F}(J)\cdot\mathcal{F}(M_r)\right)\right)} ,$$

where J denotes an array of ones of the same size as M_p, $\mathcal{F}(\cdot)$ denotes the Fast Fourier transform, and $\Re(\cdot)$ extracts the real part of a complex argument. For the PB data, a radius $r = 52$ µm, was chosen. This workflow has been adapted from (11).

Short-range Order of DG Granular Cells Apart from cell density and the shape of the DG band, the local short range order of granule cells can be analyzed, similar to structural analysis of liquids or amorphous solids in condensed matter. Such an approach based either on the pair-correlation function $g(r)$ or its Fourier transform given by a structure factor $S(q)$ was already adapted in (11) for the granule layer of human cerebellum. Here, we used the structure factor

$$S(\mathbf{q}) = \left\langle \frac{\mathbf{1}}{\mathbf{N}} \cdot \left| \sum_{\mathbf{j=1}}^{\mathbf{N}} \mathbf{e}^{\mathbf{i q \cdot p_j}} \right|^{\mathbf{2}} \right\rangle_{\phi,\theta} ,$$

computed for an array of points $\mathbf{q}$ in Fourier space (scattering vectors) based on the spatial COM coordinates $\mathbf{p}$ of the DG cell nuclei (segmentation masks of PB data), with the total number of cells N. After radial averaging in $\mathbf{q}$-space, the structure factors $S(\mathbf{q})$ are presented in Fig. S3(g). Solid lines (red, green) are given by the group-wise (AD, CTRL) median, with half-transparent areas covering the 1σ-intervals of each group.

Segmentation of DG Cell Nuclei For the PB data, segmentation of DG cell nuclei was carried out using the *Blobfinder*-tool of the segmentation and visualization package *Arivis* (Arivis AG, Germany). To this end, the *Draw Object*-tool was first used to roughly restrict the ROI to the DG. The *Blobfinder* was then applied to this volume (diameter: 7.2 µm, probability threshold: 18.3%, split sensitivity: 30.9%). Subsequently, the *Feature Filter* was used to remove objects of size ($\leq 2.5 \cdot 10^3$ µm^3), sphericity (≤ 0.25) or intensity. Finally, a python script was written to remove cells outside the DG band based on criteria involving next-neighbor distances.

The CB data, in which the DG cell nuclei are much better resolved, required a more detailed object mask, retrieved as follows: First, 6 datasets were segmented with the interactive software package Ilastik (30), and a further manual optimization based on image filters and object removal based on visual control. These segmentations served as ground truth input for machine learning based on convolutional neural networks (CNN) implemented via the *Deep-learning V-net*, which is the three-dimensional generalization of the U-net design (31). Here, the architecture from (32) was adapted, where four data sets have been used for training, two for validation. The Adam optimizer together with the dice loss function was monitored in the training procedure to cope with the class imbalance between cell and background voxels. In order to account for differences in image quality, data augmentation was applied. Further, a revised ground truth was obtained iteratively in parallel with V-net training: output probability maps were thresholded (individually for each sample), fine-tuned (manually), and used as revised ground truths. Training was carried out on a single NVIDIA Quadro RTX 8000. To fit the GPU memory, data sets were rebinned to a size of 512^3 voxels, from which single subvolumes of 256^3 voxels were used for both training and validation data, resulting in a binary dice coefficient on the validation set of 81%.
Note that for the volume rendering of the DG band and β-amyloid plaques in Fig. 1(d), data segmentation was solely based on the Ilastik software.

Structural Parameters of DG Cell Nuclei For segmented nuclei of the DG cells, five features were selected for further analysis, and computed based on the segmentation mask for each individual: median (over DG neurons) of the nuclear electron density ρ, normalized nuclear electron density variance $s = \sigma^2/\bar{\rho}^2$ (heterogeneity parameter), nuclear volume v, nuclear sphericity φ (shape parameter), and number of neighbors nn in a radius of 13.5 µm, a value selected in between first and second coordination shell of the pair correlation function $g(r)$, see also (11). The pairwise similarity (or equivalently distance) between the one-dimensional histograms (separately for each feature, Fig. 6) was computed using the 1d-Wasserstein metric W of order $p = 2$, as implemented in (33). In addition, we also computed distances based on the *Kullback-Leibler-Divergence* (*KLD*), defined as (34–36).

$$KLD[h(\beta)||h(\alpha)] = \sum_{i=1}^{N} h(\beta_i) \log\left(\frac{h(\beta_i)}{h(\alpha_i)}\right) . \quad [2]$$

In most cases, this yielded similar results, but with the additional problem of the *KLD* being ill-defined for zero values of the discretized probability distributions (zero bins). The metrics/measures were applied to each two histograms $h(\alpha)$, $h(\beta)$ with $N = 70$ bins resulting from $\sim 10^4$ objects per subject and feature. Also note that $h(\alpha)$ and $h(\beta)$ have been normalized prior to input.
Furthermore, based on the PB datasets which span a much larger FOV than the CB, further parameters have been computed and are presented in the lower part of Tab. 1 in the main article. These parameters concern the overall DG band structure, and not single DG cells. (i) From the 3d local cell density masks (defined in the SI Appendix, Methods "Computation of Local Cell Density"), median and standard deviation of the local cell density are denoted by $\bar{\rho}_n$ and ζ_n, respectively. ζ_n is also referred to as "local density fluctuations", and is an indicator for possible local defects. (ii) The DG band width d_{DG} of each data set is based on the binary 3d-mask of the DG, to which then a distance analysis tool has been applied: for each voxel within the DG, this yields the distance to the closest voxel outside the DG. The central line, extracted by skeletonization, indicates the local thickness, from which the median is computed to obtain d_{DG}. (iii) Analysis of the structure factor (see SI Appendix, Methods "Short-range Order of DG Granular Cells") yields the next-neighbor distance d_{NN}.

Presentation of Gaussian Ellipsoids The point clouds in n dimensions (nd) were described by nd ellipsoids, obtained as follows: the $n \times n$-covariance matrix and the respective nd-vector of mean values were obtained for a given point cloud. An ellipsoid was then centered around the mean (or equivalently the COM) of the point cloud, with ellipsoidal half axes (magnitude and directions) given by the eigenvectors of the covariance matrix (square root of eigenvalue and unit eigen vector). This is equivalent to least-square fitting to a multi-dimensional Gaussian distribution, with standard deviation (1σ-interval) represented by the half axes of the ellipsoids. The graphical functions were implemented with MATLAB functions presented in (37).

Analysis based on Optimal Transport In the Gaussian approximation each individual is represented by a normal distribution $\mathcal{N}(\Sigma, \mu)$ with covariance matrix Σ and mean μ. The Bures metric between two covariance matrices is given by (38, 39)

$$\mathcal{B}(\Sigma_\alpha, \Sigma_\beta) = \sqrt{tr\left(\Sigma_\alpha + \Sigma_\beta - 2\left(\Sigma_\alpha^{1/2}\Sigma_\beta\Sigma_\alpha^{1/2}\right)^{1/2}\right)} ,$$

and the L^2-optimal transport distance between two normal distributions $\mathcal{N}(\Sigma_\alpha, \mu_\alpha)$ and $\mathcal{N}(\Sigma_\beta, \mu_\beta)$ can be expressed as (40)

$$\mathcal{W}_2^2(\alpha, \beta) = ||\mu_\alpha - \mu_\beta||^2 + \mathcal{B}(\Sigma_\alpha, \Sigma_\beta)^2 ,$$

the optimal transport map from α to β is given by

$$T_{\alpha,\beta} : x \mapsto \mu_\beta + \Sigma_\alpha^{-1/2}\left(\Sigma_\alpha^{1/2}\Sigma_\beta\Sigma_\alpha^{1/2}\right)^{1/2}\Sigma_\alpha^{-1/2} \cdot (x - \mu_\alpha) .$$

For point clouds, optimal transport plans between the normalized empirical measures were computed with entropic regularization and the Sinkhorn algorithm using the implementation of (41), with a final regularization parameter of $\varepsilon = 10^{-6}$ and a plan threshold of 10^{-10} which results in high quality approximate solutions where the scale of entropic blur is considerably below the typical nearest neighbour distance of the point clouds. Local linearization of the optimal transport metric is performed as described in (42), including the approximate extraction of an optimal transport map T from the optimal transport plan between two point clouds. In the Gaussian approximation, the optimal transport center of mass ("barycenter") was used as reference for linearization, which can be computed efficiently with the fixed-point algorithm of (43). For point clouds we sampled 10^4 points from the Gaussian barycenter as an approximate reference point. SVM-classification was done with the implementation of (44). Note that we only used a *linear* (i.e. without kernel functions) SVM on four PCA-modes to avoid any risk of overfitting. Our main motivation was to extract a robust discriminating axis that lends itself to subsequent medical interpretation.

SI Additional Datasets and Analysis

DG Cell Nuclei. Fig. S2 presents additional plots on the statistical analysis of DG cell nuclei (CB data). This includes the histograms (violin plots) shown in (a) for the structural parameters ("features") volume v, sphericity φ and next neighbors nn within a radius of 13.5 µm, which are not shown in the main manuscript, for reasons of space restrictions. In (b), a correlation matrix is presented showing the correlation between any two elements of the set of features, for all subjects. Noteworthy are a positive correlation between density and volume ρ & v, and a negative one between heterogeneity and sphericity s & φ, i.e. large nuclei tend to be denser, and nuclei with larger heterogeneity (higher heterochromatin-to-euchromatin-ratio) tend to be more elongated and hence less spherical. These correlations are observed for all subjects. In (c), the "distance charts" (Wasserstein-metric, W) between individuals are shown for all features except ρ, which had already been included in the main manuscript. These heatmaps again convey the large inter-subject variation within and across groups. This is further quantified by the corresponding plots of W values (for each feature), computed for single individuals with respect to their entire group population. For the heterogeneity parameter s, the in-control-group distances are found to be significantly smaller than distances involving AD-data. A similar trend is found for the sphericity φ and the packing parameter nn, where the distances within the CTRL group are smaller than for the AD- or the cross-group case. Finally, (e) shows a graph representation (45) of distances based on the Bures-cost $\mathcal{W}$. Note that on the group-level, as shown in the main manuscript, the distances are better revealed when all features are treated jointly in the five-dimensional feature space, as quantified here by $\mathcal{W}$.

Next, Fig. S3 presents statistical analysis of DG cell nuclei, as segmented in the large volume reconstructions obtained by the PB configuration. The larger field-of-view (FOV) results in a larger section of the DG band which can be captured. Hence, in particular the width of the DG band d_{DG} and its standard deviation d_σ, as well as the local "packing" parameter nn can be well-assessed from this data. In (a), the corresponding box-whisker plots are shown. The width of the DG band is slightly widened, but does not significantly change in the AD group with respect to CTRL. Interestingly, nn seems much more tightly controlled in the CTRL group, i.e. the physiological regime, while the dispersion of nn values is much higher in the AD group, i.e. the local ordering differs substantially between members of this group. In (b), the feature histograms are presented for all patients in form of a violin plot. Since the larger FOV compared to CB configuration comes at cost of resolution, a segmented nucleus is now sampled by much fewer voxels, and the structural features within the nuclei are no longer well-assessed. In particular, we cannot expect the variance in electron density, i.e. the heterogeneity parameter s, to capture the sub-structure of the nucleus. Also, volume v and sphericity φ can be extracted only with much higher sampling errors. The corresponding "sampling artifact" also introduces bias in estimating v and φ, as can be seen by comparison with the high-resolution CB data which can be regarded as "ground truth". This may also affect the correlation plot of v, φ and s, which are shown in (c), and the corresponding W-metric, calculated for 1d-feature distributions between each two individuals as shown in (e), and

presented as box-whisker-plots for inter- and intra-group behavior, see (d). Contrarily, the results of ρ and nn, also depicted in (d-e), can be considered robust with respect to sampling. Here we note that in particular, the distances (W) within the CTRL group are much smaller than within the AD group or across groups, again indicating a much more tightly controlled parameter nn in the physiological regime, and a possible positional disordering effect of DG neurons in AD. The smaller distances between patients of the CTRL group is confirmed by the distance chart shown in (f), presenting the 5d Bures-cost $\mathcal{W}$. However, we have to keep in mind that also poorly sampled features contribute here. In (g) more analysis is included on the local packing. Instead of counting the number of neighboring neurons (nuclei) within a certain shell, as for the definition of nn, we now ask for the typical distance distribution of neighbors, as described by a structure factor $S(\mathbf{q})$ computed from the nuclear positions, see SI Appendix, Methods above. Compared to CTRL, the AD-curve shows a broader dip and a less prominent peak, indicative of a reduced short range order of nuclear positions. In addition, the AD group exhibits larger inter-subject variation, as illustrated by the shaded 1σ-intervals, again underlining a tighter control of DG structure in CTRL than in AD.

Cornu Ammonis 1. Fig. S4 summarizes the analysis of pyramidal neurons in the CA1 region. *Post mortem* biopsy punch samples from 8 different subjects were scanned: 3 subjects diagnosed with AD (based on ABC score; subjects 2, 6 and 21, aged 78 ± 11 years), 4 subjects of the control group (subjects 16, 17, 20 and 22, aged 66 ± 20 years), and a further sample (subject 12). For this purpose, all samples were collected from the same location within the hippocampus. The segmentation of neurons was carried out as detailed in SI Appendix, Methods. The segmentation quality is illustrated in Fig. S4(a). Here, gold-rendered structures mark voxels included in the segmentation mask. In (b), histograms for the same structural features as for the DG-analysis in the main text were evaluated: (1) median of electron density ρ ($\mathrm{e}^-/\mu\mathrm{m}^3$), (2) its relative variance $s = \sigma^2/\overline{\rho}^2$, (3) object volume v and (4) sphericity φ, as well as (5) number of neighboring neurons nn within a radius of 120 µm. Fig. S4(c) illustrates the correlations between different features. For example, in all subjects, smaller volume of the pyramidal neurons correlates negatively with sphericity. Visual inspection of the histograms in (b) may indicate a slight group-specific segregation for φ and nn. This is corroborated, when taking the distances between the entire feature histograms into account (W), either in form of the distance chart (Fig. S4(d)), or by comparing distances for single individuals with respect to their overall group distribution (Fig. S4(e)). Again, φ and nn show a marginally significant pattern, while the other features are dominated by the inter-subject variation with no significant effect on the group level. Fig. S4(f) and (g) illustrate the Bures-cost, taking all features into account. While this completes the analysis, we must be cautious about drawing conclusions here, since only 3-4 subjects of each group have been measured, and including a younger patient (aged 37 years). Further, datasets have been recorded at slightly different configurations, in particular regarding the X-ray energy and WG-optics, which may result in different image quality.

Multiscale Implementation. The multiscale implementation presented in the main article includes the stitching of many individual tomographic scans. For completeness, Fig. S5 presents a full slice through the entire 7×7 tomographic reconstructions (stitched) covering the entire 8 mm cylindrical punch of hippocampal tissue recorded in PB configuration.

Hydrated Tissue. While formalin-fixed paraffin-embedded (FFPE) tissue which is the standard in histology and pathology has been used for this work, we have also explored the image quality for hydrated (PBS), formalin-fixed tissue. Fig. S6 shows a corresponding reconstruction (CA1 region, CTRL group, CB configuration). While the noise is higher than for FFPE-preparation, we can still well recognize cellular bodies, nuclei and apical dendrites of the pyramidal neurons. Interestingly, tissue gaps around neurons are also observed at this stage of sample preparation, without any tissue dehydration or paraffin embedding.

Translation to Laboratory µCT. In view of future applications of the approach presented here for neuro-pathology it is important to know to which extent PC-CT can be translated to laboratory μCT instrumentation, more readily available in a clinical setting. Fig. S7 shows reconstructions from laboratory datasets, acquired with a µPC-CT setup (46, 47). X-rays were generated by a liquid-metal jet source (Excillum Inc.) with $K_{\alpha,\mathrm{Ga}} = 9.5$ keV. The sample and detector stages were fully motorized. Scans were recorded in two different configurations, serving a multiscale implementation: Overview scans with 7.7×9.7 mm^2 FOV and $px = 5$ µm, were realized using a Dexela flat panel CMOS detector (150 µm, 75 µm pixels) and large magnification ($z_{01} = 121$ mm, $z_{02} = 1.82$ m). In this configuration, the X-ray source was operated at 70 kV, 100 W, and 9×9 µm^2 source spot size (circular). 1201 projections were recorded over 185°, each with 5×1 s acquisition time. For the high-resolution configuration, the sample stage was moved to $z_{01} = 158$ mm, and a Rigaku XSight Micron detector (lens-coupled CCD, 10×optics, 5.5 µm pixels) was installed at $z_{02} = 193$ mm, resulting in a FOV of 1.2×1.6 mm^2 and $px = 0.46$ µm. Source settings were adjusted to 40 kV, 57.7 W, and 10×10 µm^2 source spot size (circular). In this configuration, 1001 projections over 181° with 1 s were acquired. Phase retrieval was performed with *Modified-Bronnikov algorithm (MBA)* (48, 49) and *Bronnikov-aided correction (BAC)* (50). For overview scans, $\alpha = 0.025$, $\gamma = 1$ and for high-resolution scans, $\alpha = 0.005$ and $\gamma = 1$ were chosen. Further data processing was carried out as presented in the main text, i.e. with the wavelet ring correction in overview scans and the additive filter in high-resolution, followed by FDK-based tomographic reconstruction.

Table S2. Optical configuration and parameters for multiscale PC-CT.

Configuration	EB	PB	CB
X-ray optics	KB & pinhole	-	KB & Waveguide (Si/Ge)
Detector	sCMOS with 50 µm-LuAg-scin., $2\times$optics	sCMOS with 50 µm-LuAg-scin., $10\times$optics	sCMOS with 15 µm-Gadox-scin.
z_{02} / z_{01} (mm)	5400 / 5060	220 / $88 \cdot 10^3$	5100 / $125 = M \approx 41$ or 5100 / $40 = M \approx 128$
FOV h$\times$v (mm^2)	8.3×6.7	1.7×1.3	0.4×0.4 or 0.13×0.13
px (µm)	3.06	0.65	0.162 or 0.051
F	0.3240	0.0220	0.0013 or 0.0008
Number of projections	1×2000	1×1500	1-4×1501
Number of empty beam projections	100	150	1-$4 \times 2 \times 100$
Exposure time per projection (s)	1	0.035 (cont.)	≤ 1

Table S3. Phase retrieval and reconstruction parameters.

Configuration	EB	PB		CB			
Energy (keV)	13.8	13.8	8.0	8.0	13.8	8.0	14.8
px (µm)	3.06	0.65	0.65	0.123	0.167	0.200	0.051
Phase retrieval *	CTF (1)	CTF (1)	CTF (1)	CTF (1/3)	CTF (4)	NLT (1)	NLT (4)
δ/β	20	33	30	35 / 50	35	130	115
Tomography	FBP	FBP	FBP	FBP	FDK	FBP	FBP
Ring removal	W	A	R	A/W	A	A/W	A
FSC (µm)	6.4	4.2**	1.6	0.963	0.385	1.268	0.219
Fig.	1(c)	2(a)	-	-	5	2(c)	2(d)

* number of measurement planes. ** local tomography (8 mm-biopsy punch).

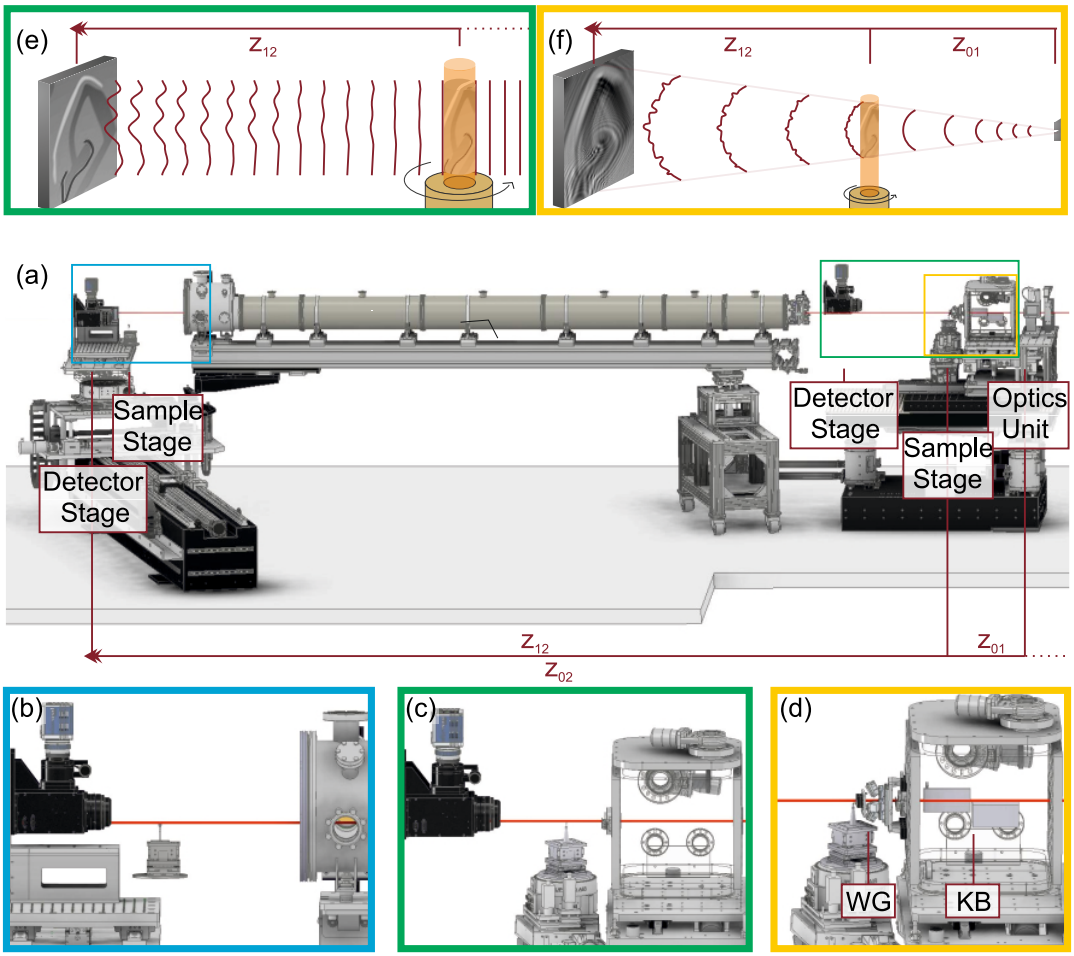

Fig. S1. Schematics of the setups. (a) Overview of the GINIX-endstation for multiscale PC-CT: direction of X-rays travel is from right to left. Depending on the configuration (marked by colored boxes), either of two sample and detector stages is utilized. (b) In EB configuration, the stages installed further downstream are used. Note that the optics unit - not shown in this zoom-in - shapes the beam via the KB mirrors and a pinhole. (c) In PB configuration, optics from the optics unit are removed, and the upstream stages are inserted. (d) In CB configuration, again KB mirrors focus the X-rays onto a CB. The sample installed at the upstream sample stage is imaged with the camera > 5 m downstream. (e & f) Schematics of the X-rays free-space propagation: image formation in (e) parallel-beam geometry as in (c), (f) cone-beam geometry leading to effective geometrical magnification as exploited in (d).

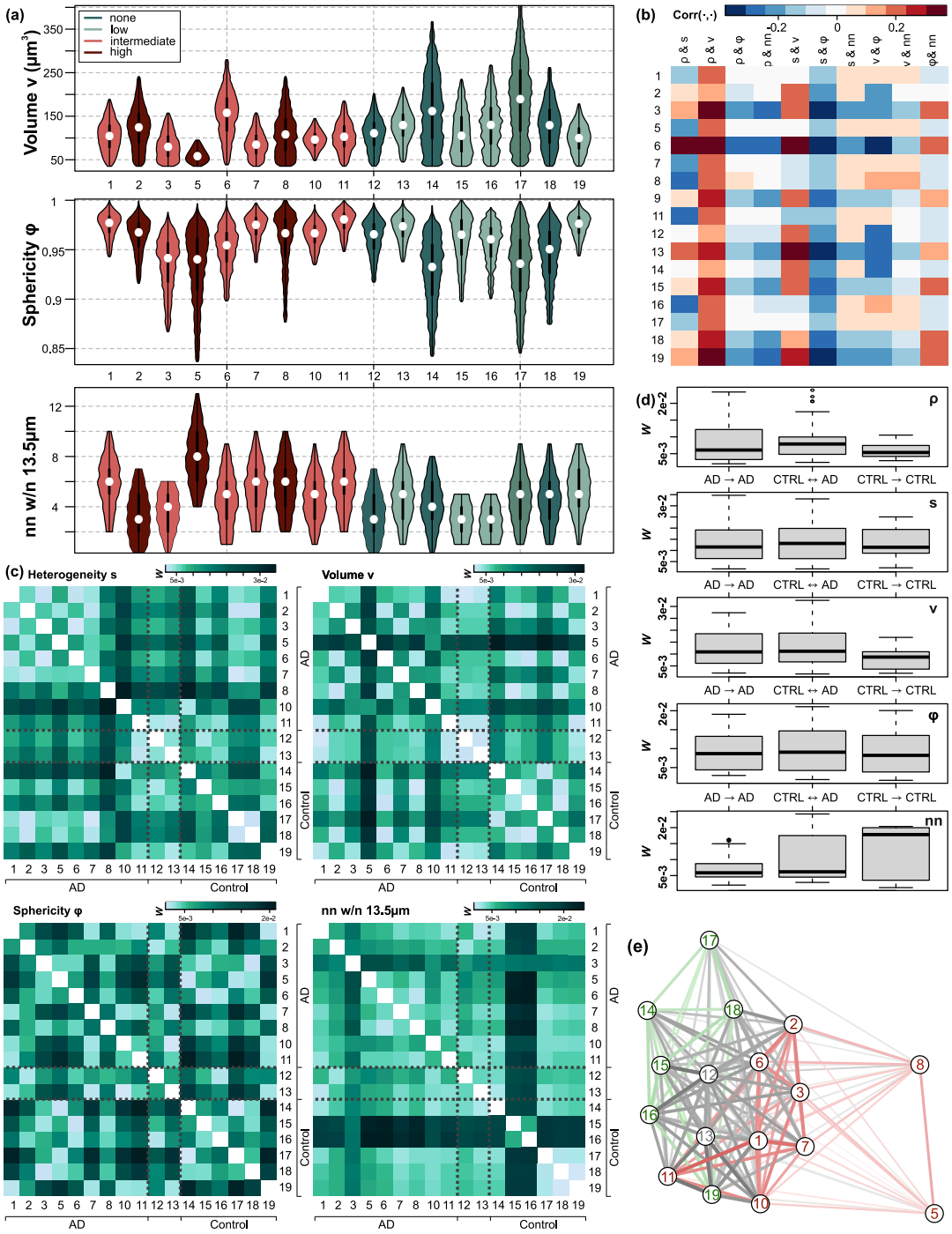

Fig. S2. Nuclei of DG granular cells – supplementary analysis of CB data. (a) Violin plots of structural features for each subject, (top to bottom): nuclear volume v, sphericity φ and number of neighboring objects (nn) within a radius of 13.5 µm. The color scheme corresponds to the ABC score. (b) Feature-feature correlation (columns), evaluated for different subjects (rows). (c) Matrices of Wasserstein-measures (W), (c, top left) heterogeneity parameter s, (top right) nuclear volume v, (bottom left) sphericity φ, (bottom right) nn, and (d) Scatter plots of W values, calculated for each individual with respect to its entire group (with subject 12 and 13 excluded). (e) Bures-cost $\mathcal{W}$ in 5d-space represented as a graph: bold connections and close node proximity correspond to lower $\mathcal{W}$. Connections between controls are colored "green", between AD-individuals "red" and inter-groups "gray" (including subjects with no group assignment).

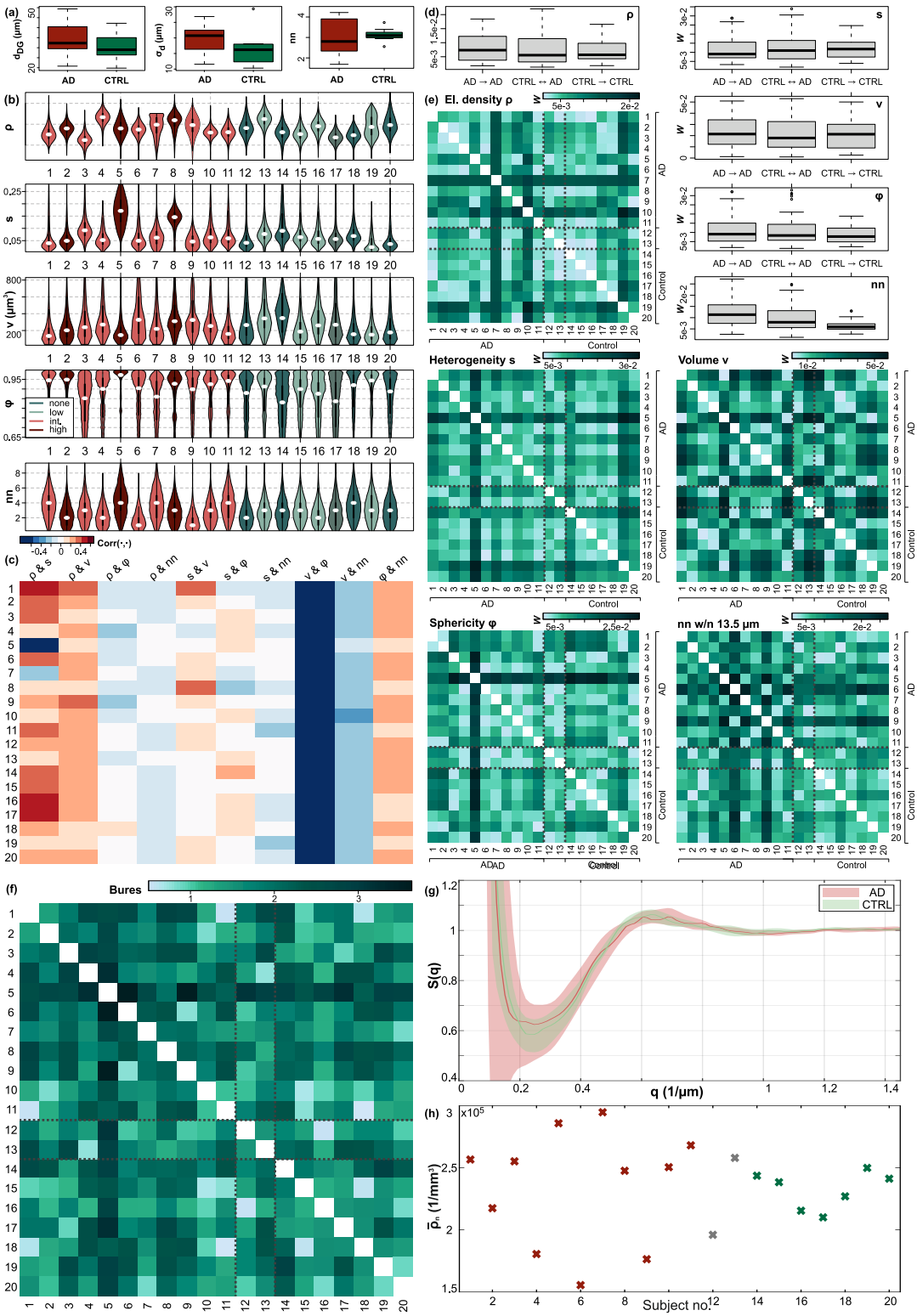

Fig. S3. Nuclei of DG granular cells – supplementary analysis of PB data. (a) Box-whisker plots of (left) granular cell bandwidth d_{DG}, (center) its variance σ_d, and (right) number of neighboring objects (nn) within a radius of 13.5 µm; each (left, red) grouped for AD subjects, (right, green) for controls according to ABC score. (b) Violin plots of structural features (top to bottom): median electron-density ρ and heterogeneity s, nuclear volume v, sphericity φ, and nn within 13.5 µm. The color scheme corresponds to the respective ABC score. (c) Feature-feature correlation (columns), evaluated for different subjects (rows). (d) Plots of Wasserstein-values (W), calculated for each individual with respect to its entire group (with the exclusion of subjects 12 and 13). (e) Matrices of W measures, for all five features. (f) Matrices of W measures. (e) Bures-cost $\mathcal{W}$ in 5d. (g) Structure factor $S(q)$ computed from the centers-of-mass of DG cell nuclei masks (see SI Appendix, Methods "Structural Parameters of DG Cell Nuclei"). Lines indicate the group-wise median, half-transparent areas the 1σ-intervals. The positions of the scattering peak indicate the next neighbor distances d_{NN}, namely $d_{\mathrm{NN}} = 13.88$ µm, and $d_{\mathrm{NN}} = 15.04$ µm, for AD and CTRL, respectively. However, the modulation of $S(q)$, i.e. the dip and the peak are less pronounced for AD, indicating a reduced short range order compared to in healthy tissue. (h) Group-averaged cell densities (red: AD, green: CTRL, gray: with no group assignment), obtained from density maps evaluated within the cell band only by applying a density threshold (10^5 1/mm^3, see SI Appendix, Methods "Computation of Local Cell Density"). AD exhibits a larger variance compared to CTRL.

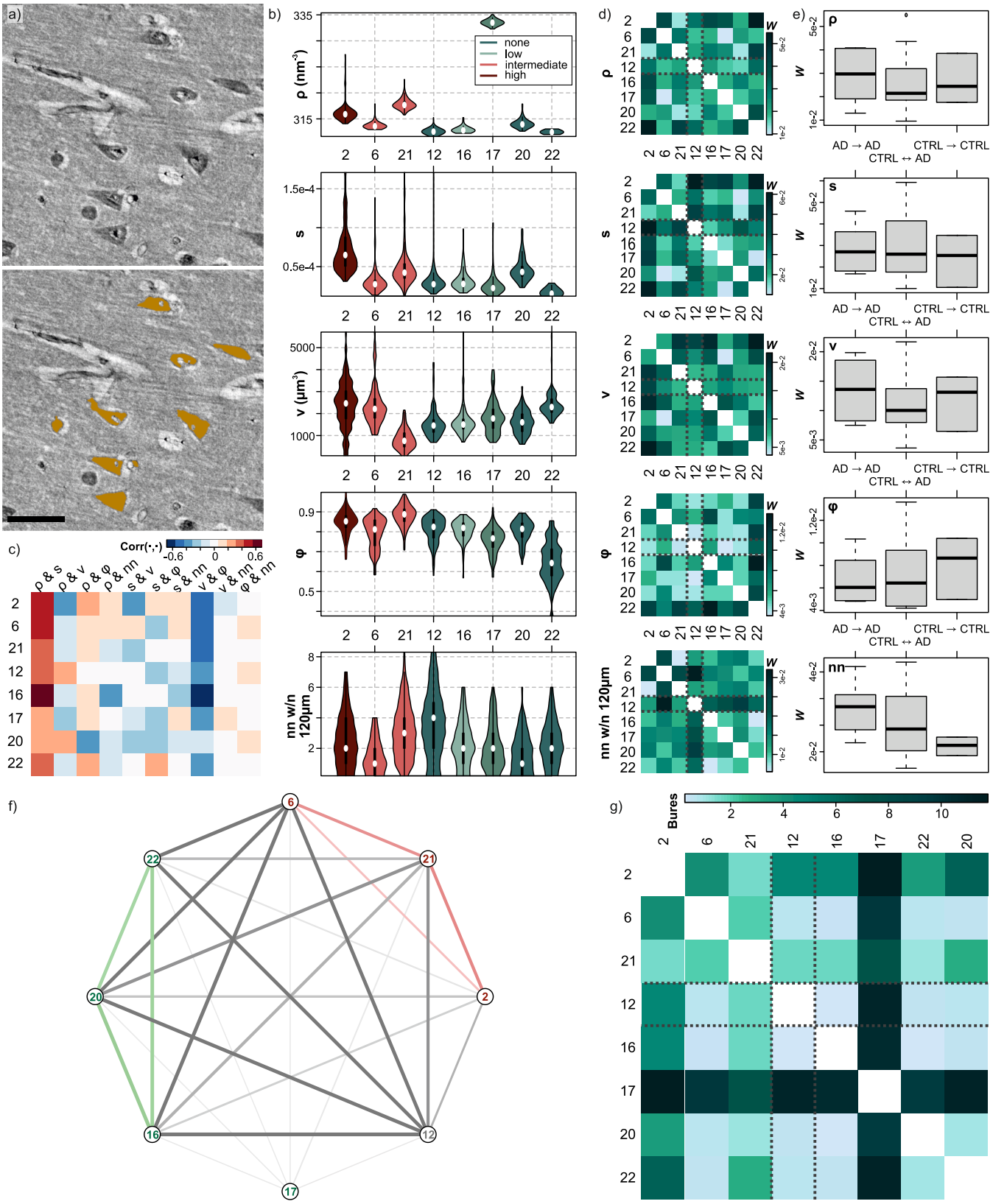

Fig. S4. Pyramidal neurons in CA1 – statistical analysis. (a) Virtual sectioning to illustrate segmentation of pyramidal neurons. Scalebar: 50 µm. (b) Violin plots of the five selected features, where the color scheme indicates the ABC score of the respective subject. (c) Feature-feature correlation (columns), evaluated for different subjects (rows). (d) Matrices of Wasserstein-measures (W), for all five features. (e) Plots of W measures, evaluated for single individuals with respect to their entire group distributions (with the exclusion of subject 12). (g) Bures-cost $\mathcal{W}$ in 5d. (f & g) Presentation of the Bures-cost $\mathcal{W}$ (computed in $5d$), (f) as graph where thicker and shorter connections indicate lower cost (red: AD, green: CTRL, gray: with no group assignment), and (g) as distance chart.

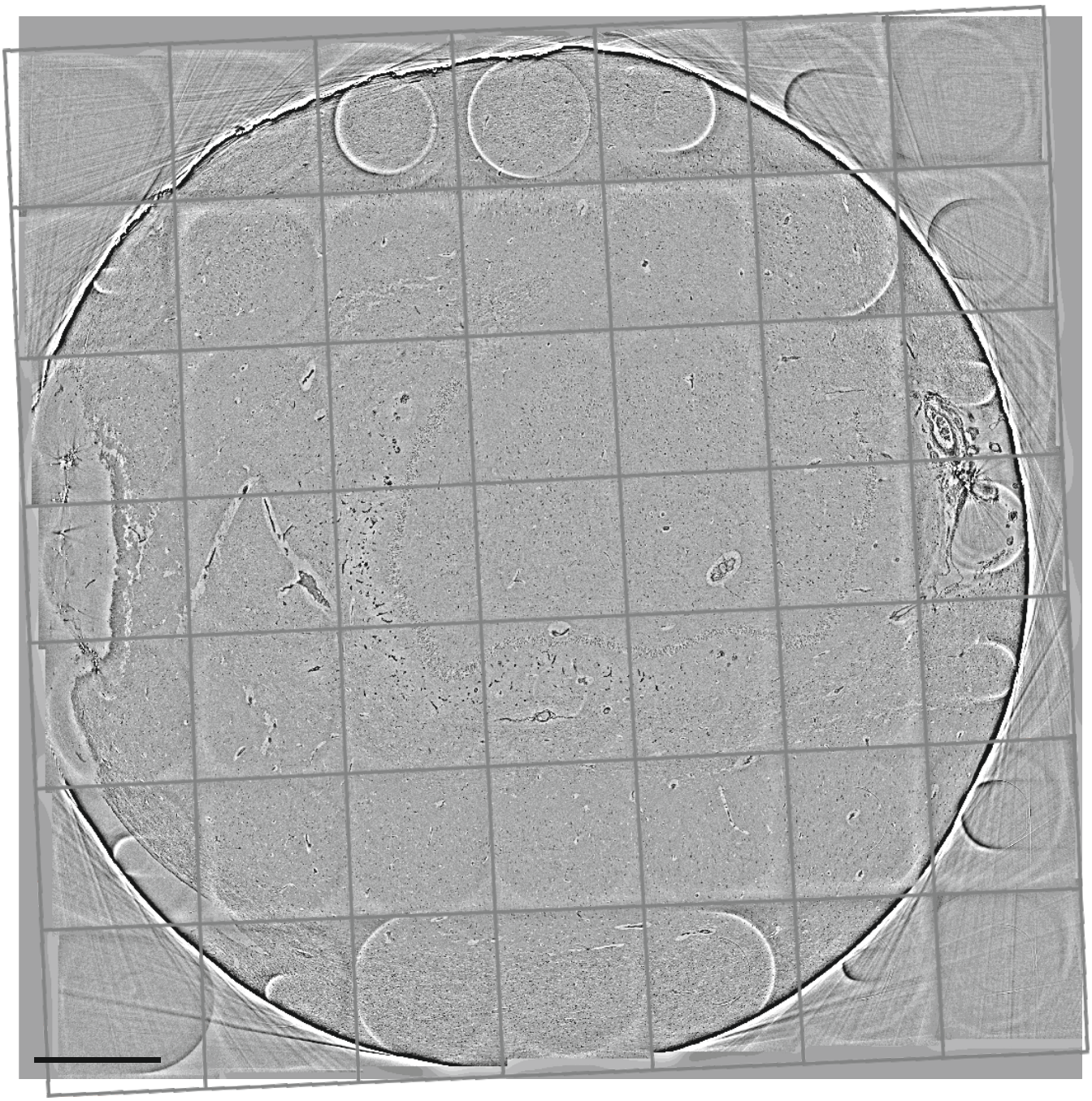

Fig. S5. Stitching of tomographic data sets for multiscale analysis. A full slice through the entire 7×7 tomographic reconstructions is shown covering the entire 8 mm cylindrical punch of hippocampal tissue recorded in PB configuration. Scalebar: 1 mm.

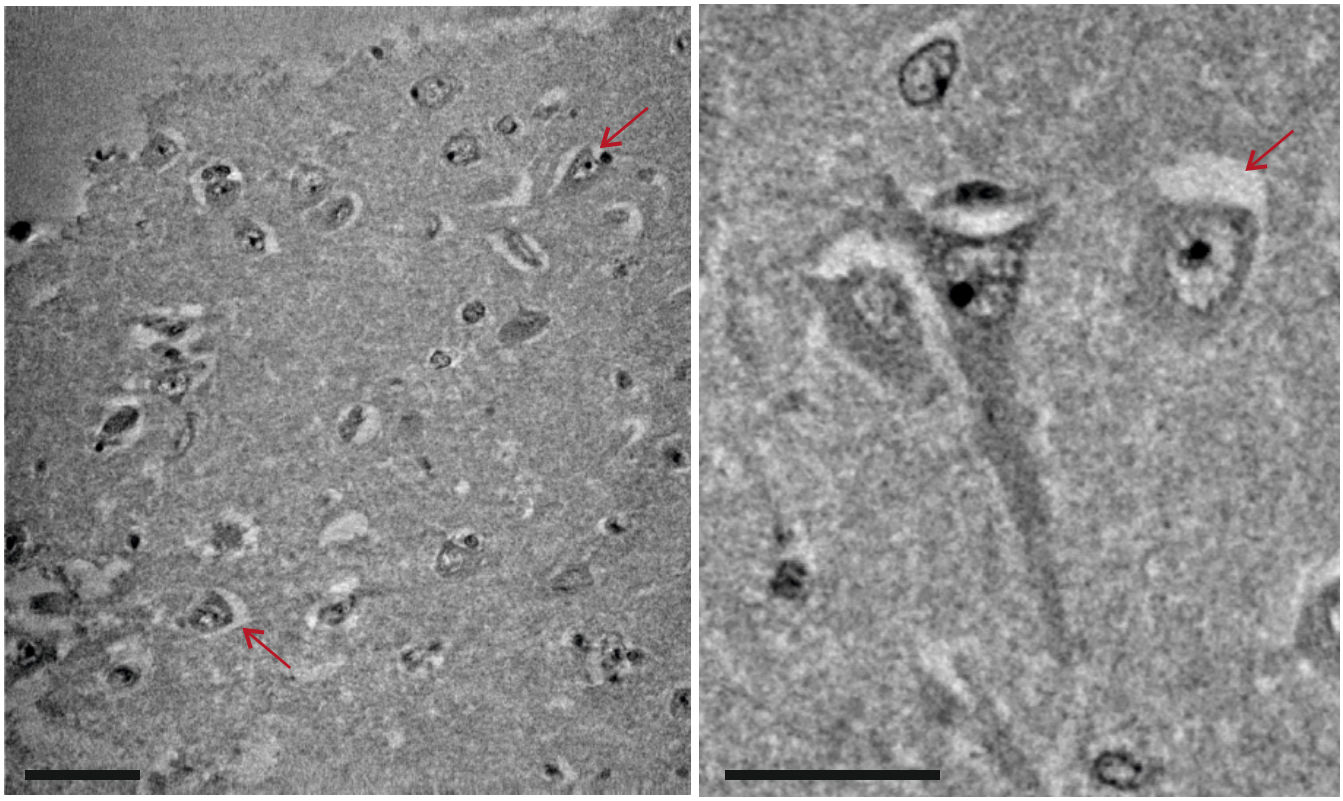

Fig. S6. Reconstruction of hydrated (PBS), formalin-fixed tissue. The example of a biopsy punch into the CA1 region (CTRL group) recorded in CB configuration) is shown, demonstrating that cellular bodies, nuclei and apical dendrites of the pyramidal neurons, are also resolved for this preparation, without tissue dehydration and paraffin embedding. Interestingly, tissue gaps around neurons are also observed at this stage of sample preparation. Scalebars: (a) 50 µm, (b) 30 µm.

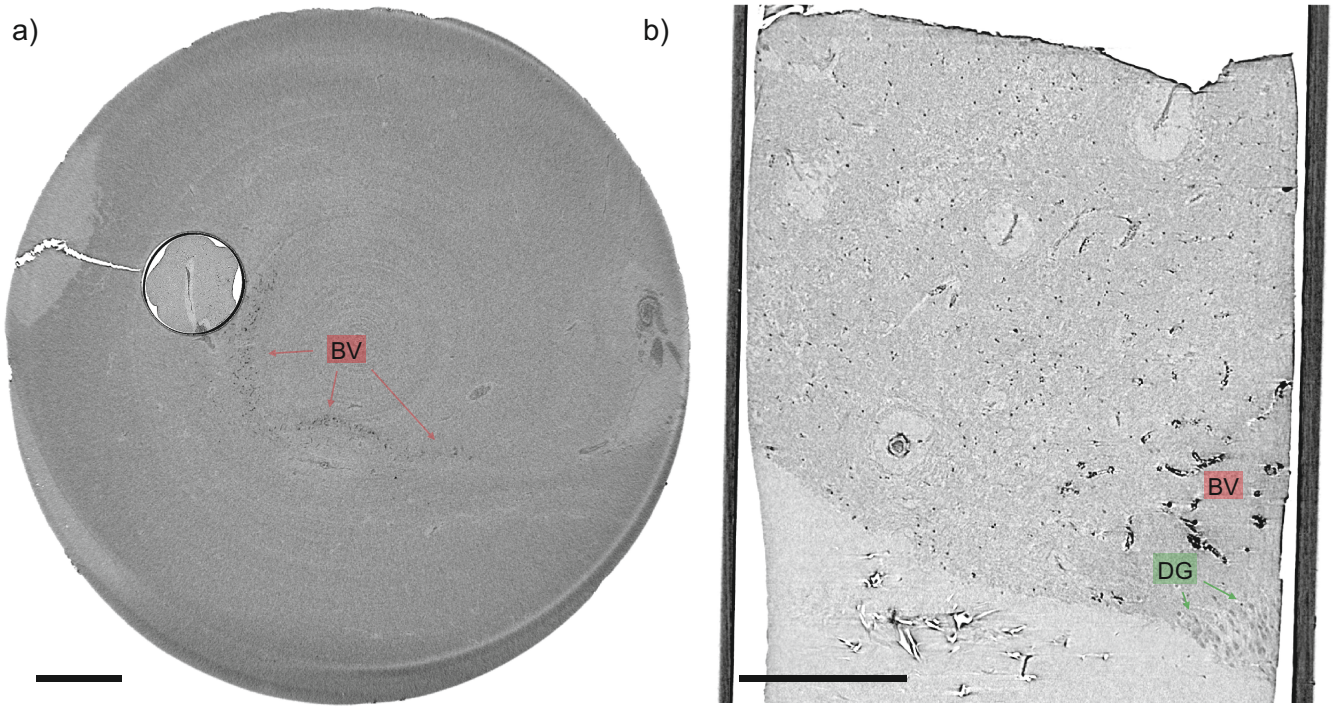

Fig. S7. PC-CT with laboratory µCT instrumentation. The same tissue block which was used for demonstrating the multiscale imaging workflow in the main text is show. Experimental details are described in SI Appendix, Methods. (a) Overview scan of the 8 mm-tissue block, with the higher resolution dataset of the 1 mm-biopsy punch merged into the volume. (b) Virtual slice through the reconstruction volume of the 1mm-biopsy punch, with labeled anatomical features such as calcified blood vessels (BV) and the DG cell band. Scalebars: (a) 1 mm, (b) 300 µm.

References

1. DR Thal, U Rüb, M Orantes, H Braak, Phases of aβ-deposition in the human brain and its relevance for the development of ad. *Neurology* **58**, 1791–1800 (2002).
2. H Braak, I Alafuzoff, T Arzberger, H Kretzschmar, K Del Tredici, Staging of alzheimer disease-associated neurofibrillary pathology using paraffin sections and immunocytochemistry. *Acta neuropathologica* **112**, 389–404 (2006).
3. SS Mirra, et al., The consortium to establish a registry for alzheimer's disease (cerad): Part ii. standardization of the neuropathologic assessment of alzheimer's disease. *Neurology* **41**, 479–479 (1991).
4. TJ Montine, et al., National institute on aging–alzheimer's association guidelines for the neuropathologic assessment of alzheimer's disease: a practical approach. *Acta neuropathologica* **123**, 1–11 (2012).
5. H Braak, E Braak, Neuropathological stageing of alzheimer-related changes. *Acta neuropathologica* **82**, 239–259 (1991).
6. T Salditt, et al., Compound focusing mirror and X-ray waveguide optics for coherent imaging and nano-diffraction. *J. Synchrotron Radiat.* **22**, 867–878 (2015).
7. K Balewski, et al., Petra iii: A low emittance synchrotron radiation source, (DESY, Hamburg, Germany), Technical report (2004).
8. J Frohn, et al., 3d virtual histology of human pancreatic tissue by multiscale phase-contrast x-ray tomography. *J. Synchrotron Radiat.* **27**, 1707–1719 (2020).
9. M Reichardt, J Frohn, A Khan, F Alves, T Salditt, Multi-scale x-ray phase-contrast tomography of murine heart tissue. *Biomed. Opt. Express* **11**, 2633–2651 (2020).
10. M Bartels, M Krenkel, J Haber, R Wilke, T Salditt, X-ray holographic imaging of hydrated biological cells in solution. *Phys. review letters* **114**, 048103 (2015).
11. M Töpperwien, F Van der Meer, C Stadelmann, T Salditt, Three-dimensional virtual histology of human cerebellum by X-ray phase-contrast tomography. *PNAS* **115**, 6940–6945 (2018).
12. H Neubauer, et al., High aspect ratio x-ray waveguide channels fabricated by e-beam lithography and wafer bonding. *J. applied physics* **115**, 214305 (2014).
13. K Giewekemeyer, H Neubauer, S Kalbfleisch, SP Krüger, T Salditt, Holographic and diffractive x-ray imaging using waveguides as quasi-point sources. *New J. Phys.* **12**, 035008 (2010).
14. SP Krüger, et al., Sub-15 nm beam confinement by two crossed x-ray waveguides. *Opt. express* **18**, 13492–13501 (2010).
15. T Salditt, S Krüger, C Fuhse, C Bähtz, High-transmission planar x-ray waveguides. *Phys. review letters* **100**, 184801 (2008).
16. LM Lohse, et al., A phase-retrieval toolbox for x-ray holography and tomography. *J. Synchrotron Radiat.* **27** (2020).
17. P Cloetens, et al., Holotomography: Quantitative phase tomography with micrometer resolution using hard synchrotron radiation x rays. *Appl. Phys. Lett.* **75**, 2912–2914 (1999).
18. S Zabler, P Cloetens, JP Guigay, J Baruchel, M Schlenker, Optimization of phase contrast imaging using hard x rays. *Rev. Sci. Instrum.* **76**, 073705 (2005).
19. L Turner, et al., X-ray phase imaging: Demonstration of extended conditions for homogeneous objects. *Opt. Express* **12**, 2960–2965 (2004).
20. WJ Palenstijn, KJ Batenburg, J Sijbers, The astra tomography toolbox in *13^{th} International Conference on Computational and Mathematical Methods in Science and Engineering. CMMSE.* (2013).
21. W van Aarle, et al., The ASTRA Toolbox: A platform for advanced algorithm development in electron tomography. *Ultramicroscopy* **157**, 35–47 (2015).
22. W van Aarle, et al., Fast and flexible X-ray tomography using the ASTRA toolbox. *Opt. Express* **24**, 25129–25147 (2016).
23. RA Ketcham, New algorithms for ring artifact removal. *Proc. SPIE* **6318**, 63180O (2006).
24. B Münch, P Trtik, F Marone, M Stampanoni, Stripe and ring artifact removal with combined wavelet-fourier filtering. *Opt. Express* **17**, 8567–8591 (2009).
25. T Butz, *Fourier transformation for pedestrians.* (Springer), (2006).
26. Cxro - the center for x-ray optics (http://cxro.lbl.gov/) (2020).
27. AL Robisch, et al., Nanoscale x-ray holotomography of human brain tissue with phase retrieval based on multienergy recordings. *J. Med. Imaging* **7**, 1 (2020).
28. TF Chan, LA Vese, Active contours without edges. *IEEE Transactions on image processing* **10**, 266–277 (2001).
29. BC Lowekamp, DT Chen, L Ibáñez, D Blezek, The design of simpleitk. *Front. neuroinformatics* **7**, 45 (2013).
30. S Berg, et al., Ilastik: interactive machine learning for (bio) image analysis. *Nat. Methods* **16**, 1–7 (2019).
31. O Ronneberger, P Fischer, T Brox, U-net: Convolutional networks for biomedical image segmentation in *Medical Image Computing and Computer-Assisted Intervention – MICCAI 2015*, eds. N Navab, J Hornegger, WM Wells, AF Frangi. (Springer International Publishing, Cham), pp. 234–241 (2015).
32. F Milletari, N Navab, SA Ahmadi, V-net: Fully convolutional neural networks for volumetric medical image segmentation in *2016 fourth international conference on 3D vision (3DV).* (IEEE), pp. 565–571 (2016).
33. D Schuhmacher, et al., *transport: Computation of Optimal Transport Plans and Wasserstein Distances*, (2020) R package version 0.12-2.
34. R Core Team, *R: A Language and Environment for Statistical Computing* (R Foundation for Statistical Computing, Vienna, Austria), (2013) ISBN 3-900051-07-0.
35. S Kullback, RA Leibler, On information and sufficiency. *The annals mathematical statistics* **22**, 79–86 (1951).

36. JM Bernardo, R Rueda, Bayesian hypothesis testing: A reference approach. *Int. Stat. Rev.* **70**, 351–372 (2002).
37. Plot_gaussian_ellipsoid (https://www.mathworks.com/matlabcentral/fileexchange/16543-plot_gaussian_ellipsoid) (year?) Accessed: 2020-12-08.
38. D Bures, An extension of kakutani's theorem on infinite product measures to the tensor product of semifinite w*-algebras. *Transactions Am. Math. Soc.* **135**, 199–212 (1969).
39. PJ Forrester, M Kieburg, Relating the bures measure to the cauchy two-matrix model. *Commun. Math. Phys.* **342**, 151–187 (2016).
40. G Peyré, M Cuturi, , et al., Computational optimal transport: With applications to data science. *Foundations Trends Mach. Learn.* **11**, 355–607 (2019).
41. B Schmitzer, Stabilized sparse scaling algorithms for entropy regularized transport problems. *SIAM J. on Sci. Comput.* **41**, A1443–A1481 (2019).
42. W Wang, D Slepčev, S Basu, JA Ozolek, GK Rohde, A linear optimal transportation framework for quantifying and visualizing variations in sets of images. *Int. J. Comp. Vis.* **101**, 254–269 (2012).
43. PC Álvarez-Esteban, E del Barrio, J Cuesta-Albertos, C Matrán, A fixed-point approach to barycenters in Wasserstein space. *J. Math. Analysis Appl.* **441**, 744–762 (2016).
44. F Pedregosa, et al., Scikit-learn: Machine learning in Python. *J. Mach. Learn. Res.* **12**, 2825–2830 (2011).
45. S Epskamp, AOJ Cramer, LJ Waldorp, VD Schmittmann, D Borsboom, qgraph: Network visualizations of relationships in psychometric data. *J. Stat. Softw.* **48**, 1–18 (2012).
46. M Bartels, VH Hernandez, M Krenkel, T Moser, T Salditt, Phase contrast tomography of the mouse cochlea at microfocus x-ray sources. *Appl. Phys. Lett.* **103**, 083703 (2013).
47. M Töpperwien, et al., Three-dimensional mouse brain cytoarchitecture revealed by laboratory-based x-ray phase-contrast tomography. *Sci. Rep.* **7**, 42847 (2017).
48. A Groso, R Abela, M Stampanoni, Implementation of a fast method for high resolution phase contrast tomography. *Opt. Express* **14**, 8103–8110 (2006).
49. A Groso, et al., Phase contrast tomography: An alternative approach. *Appl. Phys. Lett.* **88**, 214104 (2006).
50. YD Witte, M Boone, J Vlassenbroeck, M Dierick, LV Hoorebeke, Bronnikov-aided correction for x-ray computed tomography. *J. Opt. Soc. Am. A* **26**, 890–894 (2009).